Self-organized double-wall oxide nanotube layers on glass-forming Ti-Zr-Si(-Nb) alloys

Hanna Sopha[a], Darius Pohl[b], Christine Damm[b], Ludek Hromadko[a], Bernd Rellinghaus[b], Annett Gebert[c], Jan M. Macak[a,*]

[a]*Center of Materials and Nanotechnologies, Faculty of Chemical Technology, University of Pardubice, Nam. Cs. Legii 565, 53002 Pardubice, Czech Republic*
[b]*Department of Metastable and Nanostructured Materials, Institute for Metallic Materials, Leibniz-Institute for Solid State and Materials Research IFW Dresden, Helmholtzstr. 20, 01171 Dresden, Germany*
[c]*Department of Chemistry of Functional Materials, Institute for Complex Materials, Leibniz-Institute for Solid State and Materials Research IFW Dresden, Helmholtzstr. 20, 01171 Dresden, Germany*
**Corresponding Author: e-mail: jan.macak@upce.cz*
Phone: +420-466 037 401

Abstract

In this work, we report for the first time on the use of melt spun glass-forming alloys - $Ti_{75}Zr_{10}Si_{15}$ (TZS) and $Ti_{60}Zr_{10}Si_{15}Nb_{15}$ (TZSN) - as substrates for the growth of anodic oxide nanotube layers. Upon their anodization in ethylene glycol based electrolytes, highly ordered nanotube layers were achieved. In comparison to TiO_2 nanotube layers grown on Ti foils, under the same conditions for reference, smaller diameter nanotubes (~116 nm for TZS and ~90 nm for TZSN) and shorter nanotubes (~11.5 µm and ~6.5 µm for TZS and TZSN, respectively) were obtained for both amorphous alloys. Furthermore, TEM and STEM studies, coupled with EDX analysis, revealed a double-wall structure of the as-grown amorphous oxide nanotubes with Ti species being enriched in the inner wall, and Si species in the outer wall, whereby Zr and Nb species were homogeneously distributed.

Keywords: Nanotubes, Anodization, Self-organization, Alloys, TEM

1. Introduction

Titanium and its alloys are widely used for orthopaedic implants due to their high mechanical strength, biocompatibility, and enhanced corrosion resistance compared to stainless steel or CoCr-alloys [1,2]. However, conventional alloys often contain cytotoxic elements, such as Al and V, which can be released from the alloys in biological environments [3]. Compared to crystalline alloys, glass-forming Ti alloys with amorphous structure show improved properties, e.g. higher strength, and in part, a lower Young's modulus, as well as higher wear resistance, and comparable corrosion stability. Considering this, two new glass-forming Ti alloys were developed recently, namely $Ti_{75}Zr_{10}Si_{15}$ and $Ti_{60}Zr_{10}Si_{15}Nb_{15}$ [4,5], with the aim to be used for implant applications. Both alloys showed very low corrosion rates in simulated body fluid and apatite forming ability [6]. In addition, the Nb containing alloy showed an improved glass-forming ability and mechanical properties compared to the $Ti_{75}Zr_{10}Si_{15}$ [4-6].

The surface of the implants plays an important role for their successful osseointegration. The native TiO_2 layer, which is approximately 2-5 nm thick, at the metal or alloy surface is defined as bioinert, and cannot easily bind to the bone tissue. Only thicker and more stable TiO_2 based oxide layers were shown to be favourable for the surface bioactivity [7,8]. Various surface modifications of the Ti and Ti alloys have been proposed and are currently used, e.g. thermal or plasma spraying, sparking, or anodic oxidation [2,9]. For glassy Ti alloys, those studies are still rather scarce. The Ti-Zr-Si(-Nb) alloys have recently been investigated regarding the possibility of surface modification by thermal oxidation treatment without changing the alloys microstructure [10].

Anodic oxidation is a robust solution for surface treatment yielding an oxide layer on the substrate (working electrode), with a thickness that is proportional to the applied potential between the working and counter electrodes. It is well-known that the anodization of Ti leads to the formation of TiO_2 nanotubes when using fluoride containing electrolytes [11-14].

Furthermore, during the last years, it was shown that also other valve metals, such as Zr [15-17] and Nb [18,19], and several Ti binary [20-22], ternary [23,24] and quaternary alloys [25,26] can be anodized to nanotubular or nanoporous structures in fluoride containing electrolytes. The nanotubes grown on these alloys are similar to pure TiO_2 nanotubes. They can show interesting properties depending on the anodization conditions. For instance, on some of these alloys, nanotubes with different scales were developed during anodization at a constant potential [22,23,25,26]. Moreover, in case of the binary Ti-35Zr alloy nanotubes with alternating compositions were observed when the fluoride content in the electrolyte was changed [20]. To the best of our knowledge, all these substrate materials had a crystalline structure.

In this work, for the first time two glass-forming Ti alloys - $Ti_{75}Zr_{10}Si_{15}$ and $Ti_{60}Zr_{10}Si_{15}Nb_{15}$ - were anodized in an ethylene glycol based electrolyte to obtain nanotube layers. As the alloys have an amorphous structure, they have naturally no grain structure. This is especially interesting since for the anodization of crystalline Ti, the grain structure plays an important role regarding the nanotube uniformity [27,28]. The dimensions of the obtained nanotubes were compared with those obtained on reference Ti substrates, and differences in the current transients were analysed.

Transmission electron microscopy (TEM) and scanning transmission electron microscopy (STEM) analyses, combined with energy dispersive x-ray spectroscopy (EDX) measurements were carried out on different regions along the nanotube walls, to analyse their structure and composition in detail.

2. Experimental

Ingots of alloys with nominal compositions $Ti_{75}Zr_{10}Si_{15}$ (TZS) and $Ti_{60}Zr_{10}Nb_{15}Si_{15}$ (TZSN) (atomic-%) were prepared by arc-melting a mixture of the constituent elements with high

purity (99.9%) in an argon atmosphere. The ingots were re-melted 5 times to achieve chemical homogeneity. Single Cu-roller melt-spinning under highly purified argon atmosphere was used to produce melt-spun ribbons, with ~40 μm thickness and 3-4 mm width. Chemical analysis by means of inductively coupled plasma-optical emission spectroscopy (ICP-OES) confirmed that the real bulk composition of the ribbons matches well to the nominal one. More details of ribbon preparation and characterization are given in [5]. From melt-spun materials, ribbon samples with a length of 1.5 cm were cut for further experiments. Ribbons of the same size were cut from Ti foils (Sigma-Aldrich, 0.127 mm thick, 99.7 % purity) and used as references.

Before anodization all ribbons were degreased by sonication in isopropanol and acetone, then rinsed with isopropanol and dried in air. The electrochemical setup consisted of a 2 electrode configuration, using a platinum foil as the counter electrode, and the ribbons as working electrodes. The ribbons were immersed with both wheel-side and air-side into the electrolyte, with an area of 4 x 10 mm^2. The air-side of the ribbons was placed against the Pt electrode in a distance of approximately 2 cm. Electrochemical experiments were carried out at room temperature, employing a high-voltage potentiostat (PGU-200V, IPS Elektroniklabor GmbH).

An ethylene glycol based electrolyte was used containing 1.5 vol.% deionized water and 88 mM NH_4F. All electrolytes were prepared from reagent grade chemicals (Sigma-Aldrich). Before use, all electrolytes were aged for 9 hours by anodization of blank Ti substrates at 60 V under the same conditions as for the main anodization experiments [29]. For all experiments, electrolytes of the same age were employed. The alloys were anodized at 60 V for 6 hours. At the beginning of the anodization process, the potential was swept from 0 V to 60 V with a sweeping rate of 1 V/s. After anodization, the ribbons were rinsed and sonicated

in isopropanol and dried in air. The smoother air-side of the alloy ribbons was used for further analytical studies.

The morphology of the nanotubes was characterized by a field-emission SEM (JEOL JSM 7500F). Dimensions of the nanotubes were measured and statistically evaluated using proprietary Nanomeasure software. For each condition used in this work, average values and standard deviations were calculated from at least 3 different locations on 2 ribbons of each condition, with a high number of measurements ($n \geq 100$).

Cross sectional samples for transmission electron microscopy (TEM) were prepared by focused ion beam (FIB) cutting of lamellae using a FEI Helios nanolab 600i dual beam system (FEI EUROPE, Eindhoven, The Netherlands). The electron transparent lamella was attached to a Cu grid.

Structural and local chemical characterization was conducted by conventional and aberration-corrected high resolution transmission electron microscopy (HR-TEM) utilizing a FEI Tecnai G^2 *20* microscope (with LaB_6 emitter, scanning unit (STEM), energy dispersive X-ray spectrometer (EDXS)) and a FEI Titan^3 80-300 microscope operated at 300 kV (equipped with a field emission gun, *CEOS* CetCor image C_S-corrector, FEI DCOR probe C_S-corrector, high angle annular dark field (HAADF) detector, GatanTridiem 863ER for electron energy loss spectroscopy (EELS) and EDXS), respectively.

3. Results and discussion

3.1 Oxide nanotube growth by anodization

Ribbons of $Ti_{75}Zr_{10}Si_{15}$ (TZS) and $Ti_{60}Zr_{10}Si_{15}Nb_{15}$ (TZSN) were anodized along with Ti ribbons for reference, in an ethylene glycol based electrolyte, an electrolyte widely used for the anodization of Ti foils to obtain TiO_2 nanotube layers [12,14]. Fig. 1 shows the polarization curves and the current transients for both alloys and Ti recorded upon

anodization at 60 V for 6 h. The shape of the curve for Ti is typical for the anodization in fluoride containing ethylene glycol based electrolytes [12]. Briefly, at the beginning of the anodization process the current increased due to the formation of a compact oxide layer. The current maximum was reached already during the sweeping, at approximately 18 V. After reaching the final set potential (in this case 60 V), the current decreased rapidly. As the current minimum was reached, small pores began to develop randomly in the oxide layer, leading to a further current increase, due to an increased active area until a maximum number of pores, being transformed into separated nanotubes, was formed. Subsequently, the tubes grow in length and the current slowly decreased. Looking at Fig. 1, a similar behaviour was observed for both alloys. However, distinct differences were observed during the sweeping period at the beginning of the anodization. For both alloys, a large current plateau at nearly the same current level was found, which was in the same time the current maximum. The current dropped quickly after the constant potential of 60 V had been achieved. Other differences were observed in the position and shape of the current maximum on current transients within the following 2-3 hours of anodization (indicated by arrows in Fig. 1). For Ti, a broad peak with maximum current was recorded after approx. 1 hour of anodization. As described above, this is very typical for the anodization under these conditions [12,29]. Regarding the amorphous alloys, the recorded currents had different transients compared to Ti. After approximately 15 min of anodization, the current for the TZS alloy began to increase sharply, and reached its maximum after approximately 1 hour. The current for the TZSN alloy, however, began to increase after more than 1.5 hours, and reached its maximum after approximately 2 hours and 15 min. This could imply that a longer time was needed for the development of the nanotube structure on this Nb-containing alloy compared to the Ti and TZS. The fact that Nb slows down the nanotube development in ethylene glycol electrolytes was not described in the literature for anodization of TiNb alloys. In contrast, in an aqueous

HF containing electrolyte, longer nanotubes were grown on the Ti45Nb alloy than on the pure Ti [21], and in ethylene glycol based electrolytes a Nb content between 5 and 40 wt% in TiNb alloys did not show a significant influence on the nanotube layer thickness [30].

Beside all the above described variations in the data plots, the anodization was completed after 6 hours, with currents on approximately same level.

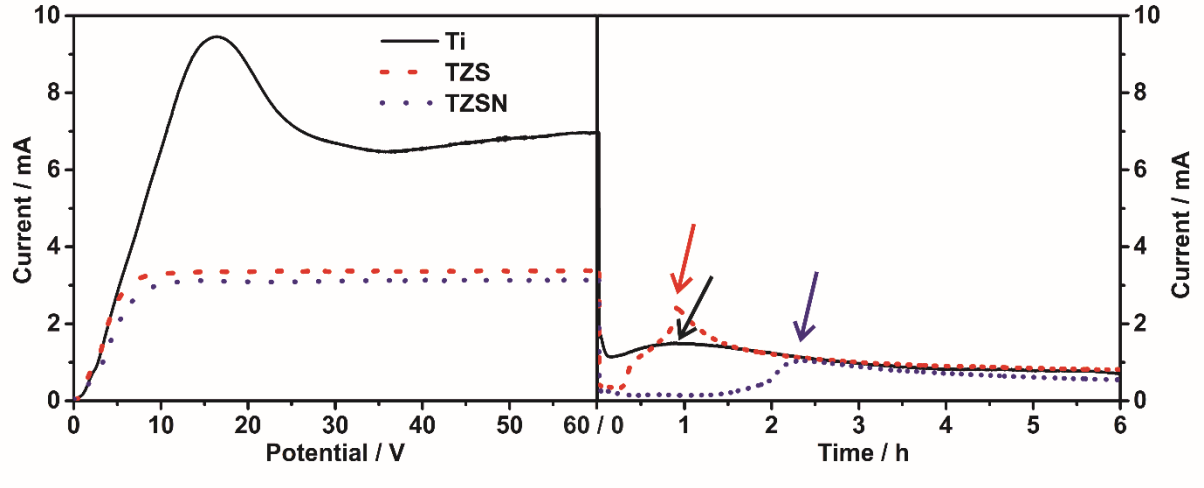

Figure 1. Polarization plots (left) and current transients (right) recorded for the anodization of the two alloys and the Ti substrate for 6 hours at 60 V. The arrows indicate the second current maximum.

3.2 Morphological characterization of oxide nanotubes with SEM

Fig. 2 shows SEM images of the nanotubes grown on both alloys after anodization described in Fig. 1. It is obvious that on both alloys, uniform nanotube layers were formed. In addition, as can be seen from the top views (Fig. 2a and 2d) and cross-section views (Fig. 2c and 2f), the nanotubes were bundled, however, only on the very top of the nanotube layers. This bundling is known from the literature for TiO_2 nanotube layers, and it is believed that it is caused by capillary forces between adjacent nanotubes during evaporative drying of the wet layers after sonication [31].

Another interesting feature of the nanotubes was the two-fold distribution of the tube bottom diameter for the TZS nanotube layer. This feature, most typically entitled "two-size scale diameter" was already reported for crystalline Ti alloys, such as the quaternary Ti29Nb13Ta4.6Zr alloy [26] or the binary Ti45Nb [22], but also for TiO_2 nanotube layers grown on Ti substrates [32]. However, in the literature, the nanotubes grown on alloys showed the two size scale on the bottom as well as on the top of the tubes. In case of TZS the differences in sizes were only observed on nanotube bottoms. This means that some of the nanotubes became wider towards the bottom, while others become smaller. For the TZSN nanotube layers, this phenomenon was not observed.

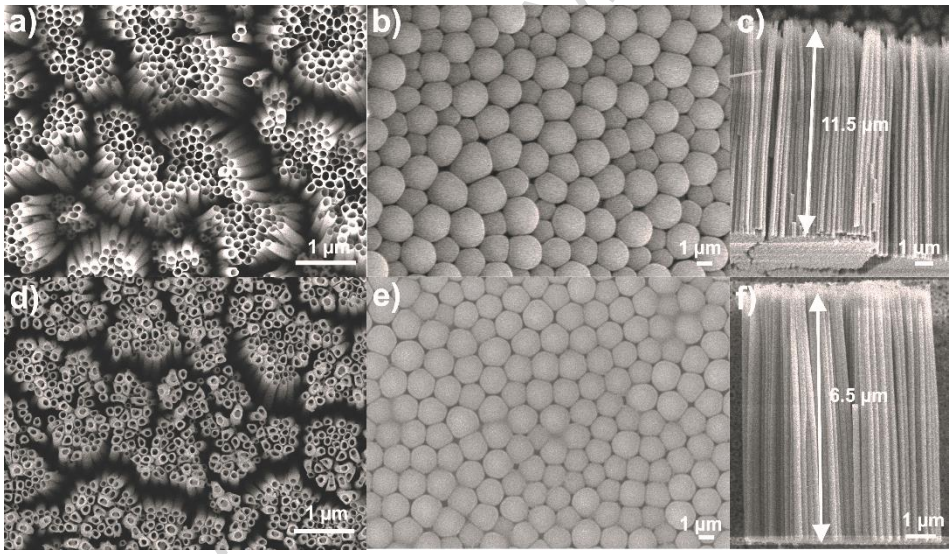

Figure 2. Top (a,d) bottom (b,e) and cross sectional (c,f) view of the alloys TZS (a,b,c) and TZSN (d,e,f).

Fig. 3a shows bar charts plotting the evaluated inner nanotube diameter and nanotube length for both alloys, and Ti as reference, after anodization at 60 V for 6 h in electrolytes of the same age. Considering the diameter, the largest inner diameter nanotubes were obtained within the TiO_2 nanotube layer with ~124 nm, followed by the TZS nanotube layer with ~116

nm. The TZSN nanotube layer exhibited the smallest nanotube diameter (~90 nm). As shown in Fig. 2b, however, the bottom parts of the TZS alloy display two-size scale of the nanotubes. Fig. 3b shows a histogram of the diameter distribution for the nanotube layers on this particular TZS alloy, obtained by analyses of SEM images taken from the bottom part of the nanotube layer.

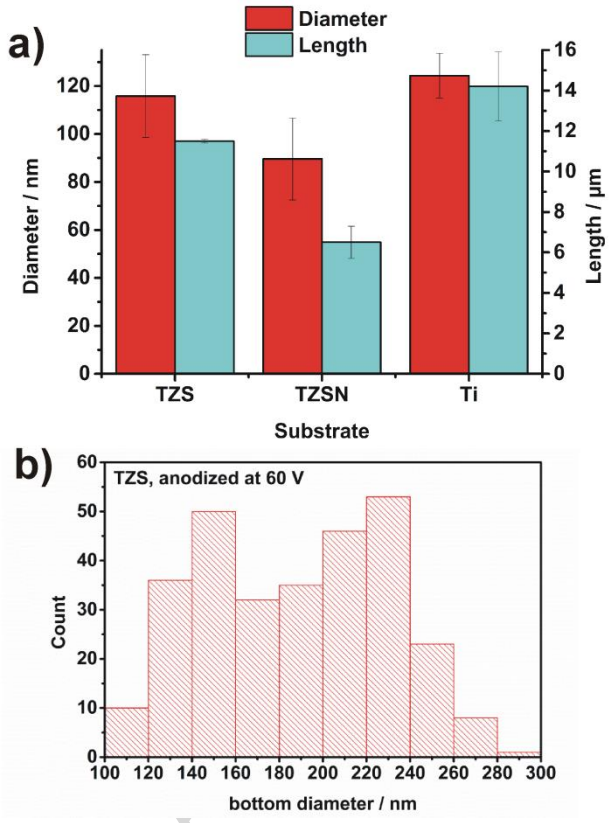

Figure 3. a) Evaluation of the average inner nanotube diameter (measured from the top of the layer) and length for the anodization of the different substrates for 6 h at 60 V; b) histogram of the bottom diameter distribution for the TZS nanotube layer.

Considering the nanotube length, the same trend was observed as for the nanotube diameter – i.e. the longest tubes of ~14 µm were grown on Ti and shortest nanotubes of ~6.5 µm on the TZSN alloy.

An explanation for these dimensional differences can be provided by different nanotube growth rates of these alloys, due to different electrochemical oxidation rates of the alloying elements and their higher stability in fluoride containing electrolytes. It was demonstrated in the Nb-oxide nanotube related literature that Nb_2O_5 is considerably more resistant than TiO_2 against dissolution in fluoride containing electrolytes. It was found that in a 1 M NaH_2PO_4 solution containing 0.5wt% HF the dissolution rate of Nb_2O_5 was 1 nm min^{-1}, whereas that of TiO_2 was 20 nm min^{-1} [21]. For Si, much harsher conditions would be required, (i.e. concentrated HF electrolytes, see Ref. [33]) to prepare porous structures compared to TiO_2 nanotube layers.

In the literature it was shown that the nanotube length of Ti-Zr alloys increases with the Zr content, while at the same time the nanotube diameter decreases. However, the impact is relatively small for Ti-Zr alloys with less than 20 wt.% Zr [34]. Looking at the dimensions of nanotube layers grown on Ti-Nb alloys in ethylene glycol electrolytes, the content of Nb does not show an influence on the nanotube length and diameter [30] within the given compositional interval. Finally, the literature for Ti-Zr-Nb reports that when Nb content is fixed and Zr content is increasing (i.e. Ti content is decreasing), the nanotube length is increasing as well (in line with the Ti-Zr literature [34]), but the diameter hardly changes [35]. The rest of the literature on Ti-Nb-Zr alloys does not compare to the results found in this study, as mostly diverse alloy composition and electrochemical conditions were used, that do not allow to see any trends. The only report on the nanotube growth on quarternary alloy having similar composition (Ti-Nb-Zr-Ta, Ref. [25]) does not contain any compositional aspect and related discussion. Finally, there is no report on the nanotube growth on Ti-Si alloys in ethylene glycol electrolytes, to the best of our knowledge.

In conclusion, it seems that the presence of Si in the alloy is the reason for shorter tubes on both presented alloys herein compared to the TiO_2 nanotubes. Even in the presence of Zr in

the alloy, that itself would lead to longer tubes on the alloy compared to pure TiO_2 nanotubes, Si seems to have a dominance for the anodization of alloys used in this study.

3.3. Structural and compositional characterization of anodized alloy surfaces with TEM

Further studies were conducted by means of TEM in order to obtain detailed information of the structural and compositional states of the oxide nanotubes grown on the $Ti_{75}Zr_{10}Si_{15}$ (TZS) and $Ti_{60}Zr_{10}Nb_{15}Si_{15}$ (TZSN) alloys, at 60 V for 6 hours. Figure 4 shows selected HR-TEM images and corresponding SAED/FFT of the bottom parts of the oxide nanotubes, and the interface region to the metallic substrate. On both alloys, TZS and TZSN, the tubes showed a similarly pronounced double wall structure. For tubes on TZS a mean total tube wall thickness of 85-90 nm and a mean inner tube diameter of 45-50 nm were estimated, while for tubes grown on TZSN those values were 70-75 nm and 25-30 nm, respectively. It has to be mentioned that the double-wall oxide nanotube structures were already reported in the literature for nanotube layers grown on Ti [36] as well as Ti-based alloys [37].

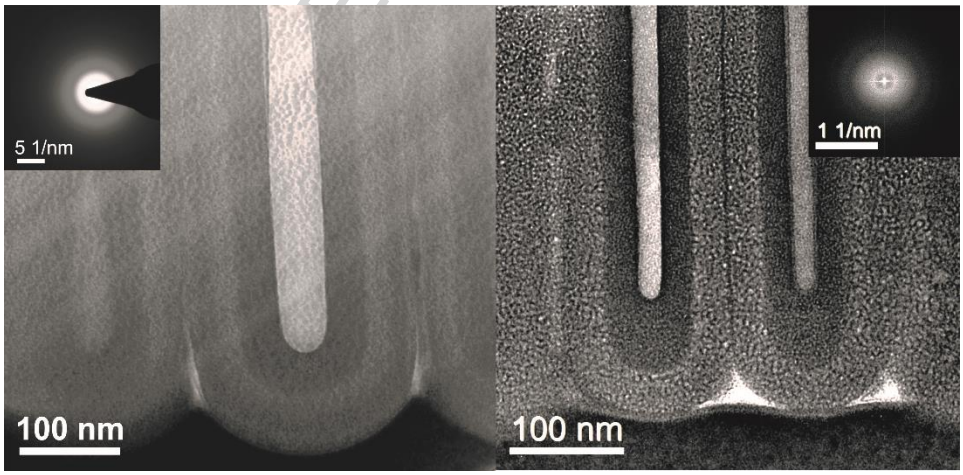

Figure 4. Bright field HR-TEM images and related SAED/FFT for oxide nanotubes grown at 60 V for 6 h on TZS (left) and TZSN (right) revealing double-wall structure.

As further apparent from Fig. 4, both walls of both alloys were amorphous. Multiple EDX analyses (using TEM) were carried out along the tube walls of TZSN oxide tubes as well as at different depths of the alloy substrate. Table 1 summarizes those typical EDX results for the constituent elements.

Table 1. EDX data reflecting the mean composition at different regions along the tube length (total tube length ~6.5 µm) obtained after anodization at 60 V for 6 hours on the air-side region of the $Ti_{60}Zr_{10}Nb_{15}Si_{15}$ (TZSN) substrate.

composition	Ti-K (at%)	Zr-K (at%)	Si-K (at%)	Nb-K (at%)
top	52.8 ± 1.2	8.2 ± 1.0	24.6 ± 1.5	14.3 ± 1.7
middle	52.4 ± 0.9	9.2 ± 1.1	22.9 ± 1.3	15.5 ± 0.6
bottom	48.0 ± 1.4	9.0 ± 1.3	31.2 ± 1.8	11.8 ± 1.7
substrate	54.0 ± 1.3	10.4 ± 0.6	18.6 ± 0.8	16.9 ± 0.9

At first, results indicated the elemental concentrations determined for the air-side of the metallic substrate (with a depth of the analysis region of ~600 nm), deviated from the nominal bulk composition of the melt spun ribbon. In particular, the Ti was depleted while the Si appeared to be enriched. The processing of the glass-forming alloy by means of single-roller melt spinning on a Cu wheel, yielded very high cooling rates but, nonetheless, a certain cooling rate gradient from the wheel-side to the air-side of the solidifying material was present. As a consequence, structural and chemical gradients were present in the alloy ribbons. Therefore, the limited glass-forming ability of those Ti-Zr-Si(-Nb) alloys yielded in a preferential precipitation of single beta-type nanocrystals within the glassy matrix on the air-side region. This was already discussed in [5]. The EDX analysis of alloy substrates in the present study, disclosed also compositional deviations at the air-side regions with local enrichment of Si as the lightest constituent.

Further, EDX analysis of the different regions of the oxide nanotubes revealed that all alloying elements contributed to the oxide nanotube growth. Ti was present in the tubes with a content higher than 50 %, thus an amorphous Ti oxide was the base compound of the tubes. But all other elements were revealed in the oxide in a similar fraction as in the metallic substrate implying that they are incorporated in the base oxide. Considering the low error

limits of this analysis method, no clear compositional gradient along the oxide tube walls was detectable.

In addition, when detailed analyses of the intensity as well as of the local structure were carried out by HR-TEM (not shown here), the atomic density of both walls seemed to be different. Therefore, oxide nanotubes on the quaternary alloy TZSN were subjected to more detailed and more precise compositional analyses using HR-TEM equipped with high-resolution EDX and STEM detectors. Analyses were devoted to the detailed chemical analysis of the amorphous double-walls of the oxide nanotubes. In Fig. 5, a HR-STEM image and the corresponding chemical maps of Ti-K, Si-K, Zr-K and Nb-K are shown. The HR-STEM image, which gave a contrast proportional to the local atomic number, confirmed also the assumption of a varying chemical composition within the double wall structure. A relatively sharp transition between the two walls, corresponding to the sharp structural transition visible in Fig. 4, was visible. From the elemental maps, it can be seen that mainly the Ti and Si concentration differed between the inner and the outer wall. The quantitative analysis of the chemical composition of the substrate (in vicinity to the nanotube), and of the inner and the outer regions of the nanotubes, is summarized in Table 2. Compared to the substrate, the inner wall showed an enrichment of Ti, while the outer wall showed a depletion. The opposite trend was found for Si, where the outer wall showed an enrichment (as compared to the substrate) while the inner wall showed a depletion. This behavior was confirmed by local EELS measurements (not shown here). Zr and Nb were homogeneously distributed in the nanotube regions (within the errors of EDX) and present in approximately same quantities as in the substrate. Reasons for this overall variation remain unclear. However, it can be speculated that this is due to different dissolution rates of metal oxides and metals in the used electrolyte. For better understanding of these variations, much more detailed analyses between electrochemical growth and detailed structural compositions (of single metals and binary, ternary and quaternary alloys of all metals) would have to be carried out. These analyses are beyond the scope of this work.

However, in literature, compositional difference between outer and inner wall have been ascribed to the decomposition of the organic electrolyte during the anodization leading to an inner C-rich tube region [38]. However, local mapping of the C-K edge using EELS (not shown here) revealed a homogeneous and quantitatively small carbon presence in the oxide tubes, and in the substrate vicinity, which is mainly caused by contaminations. Thus,

compositional fluctuations in the inner and outer amorphous tube walls can only be related to variations of all oxide concentrations.

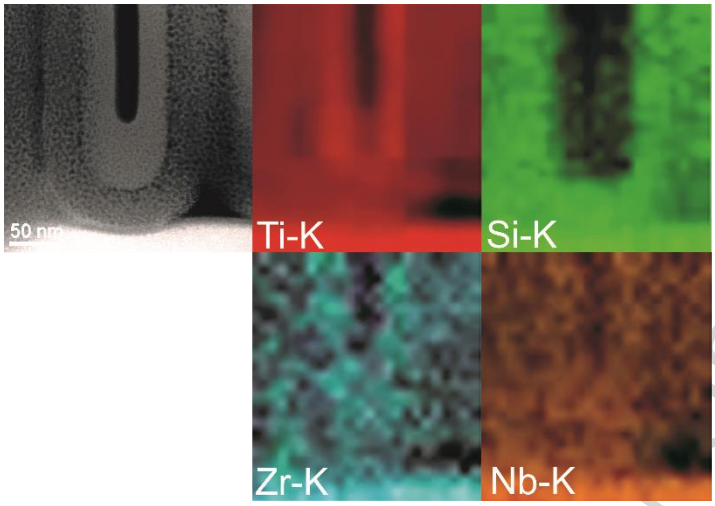

Figure 5. HR-STEM image and the corresponding chemical maps of Ti-K, Si-K, Zr-K and Nb-K of the bottom region of an oxide nanotube grown on of a TZSN substrate.

Table 2. High resolution EDX data of amorphous double-wall regions of oxide nanotubes grown on TZSN and of the TZSN alloy itself (only fitting errors are given).

composition	Ti-K(at%)	Zr-K(at%)	Si-K(at%)	Nb-K(at%)
inner wall	64.26±0.82	6.33±0.77	19.11±0.55	10.30±0.99
outer wall	51.26±0.55	5.89±0.52	34.16±0.49	8.69±0.70
substrate	56.87±0.97	4.92±0.77	26.11±0.72	10.4±1.11

Conclusions

In summary, for the first time the nanotube formation on amorphous alloys $Ti_{75}Zr_{10}Si_{15}$ and $Ti_{60}Zr_{10}Si_{15}Nb_{15}$ was demonstrated in this work. It has been shown that depending on the composition of the alloys, different nanotube dimensions were obtained when the same anodization conditions were employed. For the Nb containing alloy, nanotube layers with smaller nanotube diameter and shorter nanotube length were found. This phenomenon can be ascribed to the different oxide growth and dissolution rates of the alloying elements. Detailed HR-STEM and EDX investigations confirmed that the as-formed nanotubes on both glass-

forming alloys are completely amorphous and show a pronounced double-wall structure with different Ti and Si species distributions.

Acknowledgements

ERC and Ministry of Education, Youth and Sports of the Czech Republic are acknowledged for financial support of this work through the projects 638857 and LM2015082. The authors would also like to thank the project CZ.1.05/4.1.00/11.0251 „Center of Materials and Nanotechnologies“ cofinanced by the European Fund of the Regional Development, and the state budget of the Czech Republic.

References

[1] M. Long, H.J. Rack, Titanium alloys in total joint replacement – a materials science perspective, Biomaterials 19 (1998) 1621-39.

[2] X.Y. Liu, P.K. Chu, C.X. Ding, Surface modification of titanium, titanium alloys and related materials for biomedical applications, Mater. Sci. Eng. R 47 (2004) 49-121.

[3] M. Geetha, A.K. Singh, R. Asokamani, A.K. Gogia, Ti based biomaterials, the ultimate choice for orthopaedic implants – A review, Prog. Mater. Sci. 54 (2009) 397-425.

[4] M. Calin, A. Gebert, A.C. Ghinea, P.F. Gostin, S. Abdi, C. Mickel, J. Eckert, Designing biocompatible Ti-based metallic glasses for implant applications, Mater. Sci. Eng. C 33 (2013) 875-883.

[5] S. Abdi, M. Samadi Khoshkhoo, O. Shuleshova, M. Bönisch, M. Calin, L. Schultz, J. Eckert, M.D. Baró, J. Sort, A. Gebert, Effect of Nb addition on microstructure evolution

and nanomechanical properties of a glass-forming Ti-Zr-Si alloy, Intermetallics 46 (2014) 156-163.

[6] S. Abdi, S. Oswald, P.F. Gostin, A. Helth, J. Sort, M. D. Baro, M. Calin, L. Schultz, J. Eckert, A. Gebert, Designing new biocompatible glass-forming Ti75-xZr10NbxSi15 (x = 50, 15) alloys: corrosion, passivity, and apatite formation, J. Biomed. Mater. Res. Part B 104 (2016) 27-38.

[7] Y.-T. Sul, C.B. Johansson, S. Petronis, A. Krozer, Y. Jeong, A. Wennerberg, T. Albrektsson, Characteristics of the surface oxides on turned and electrochemically oxidized pure titanium implants up to dielectric breakdown: the oxide thickness, micropore configurations, surface roughness, crystal structure and chemical composition, Biomaterials 23 (2002) 491-501.

[8] B. Yang, M. Uchida, H.-M. Kim, X. Zhang,T. Kokubo, Preparation of bioactive titanium metal via anodic oxidation treatment, Biomaterials 25 (2004) 1003-1010.

[9] F. Variola, F. Vetrone, L. Richert, P. Jedrzejowski, J.-H. Yi, S. Zalzal, S. Clair, A. Sarkissian, D.F. Perepichka, J.D. Wuest, F. Rosei, A. Nanci, Improving biocompatibility of implantable metals by nanoscale modification of surfaces: an overview of strategies, fabrication methods, and challenges, Small 5 (2009) 996-1006.

[10] S. Abdi, M. Bönisch, S. Oswald, M. Samadi Khoshkhoo, W. Gruner, M. Lorenzetti, U. Wolff, M. Calin, J. Eckert, A. Gebert, Thermal oxidation behavior of glass-forming Ti-Zr-(Nb)-Si alloys, J. Mater. Res. (2016) DOI: 10.1557/jmr.2016.122

[11] V. Zwilling, M. Aucouturier, E. Darque-Ceretti, Anodic oxidation of titanium and TA6V alloy in chromic media. An electrochemical approach, Electrochim. Acta 45 (1999) 921-929.

[12] J.M. Macak, H. Tsuchiya, A. Ghicov, K. Yasuda, R. Hahn, S. Bauer, P. Schmuki, TiO_2 nanotubes: Self-organized electrochemical formation, properties and applications, Curr. Opin. Solid State Mater. Sci. 11 (2007) 3-18.

[13] D. Kowalski, D. Kim, P. Schmuki, TiO_2 nanotubes, nanochannels and mesosponge: Self-organized formation and applications, Nanotoday 8 (2013) 235-264.

[14] K. Lee, A. Mazare, P. Schmuki, One-dimensional titanium dioxide nanomaterials: nanotubes, Chem. Rev. 114 (2014) 9385-9454.

[15] H. Tsuchiya, J.M. Macak, L. Taveira, P. Schmuki, Fabrication and characterization of smooth high aspect ratio zirconia nanotubes, Chem. Phys. Lett. 410 (2005) 188–191.

[16] H. Tsuchiya, J.M. Macak, A. Ghicov, L. Taveira, P. Schmuki, Self-organized porous TiO_2 and ZrO_2 produced by anodization, Corros. Sci. 47 (2005) 3324–3335.

[17] S. Berger, J. Faltenbacher, S. Bauer, P. Schmuki, Enhanced self-ordering of anodic ZrO_2 nanotubes in inorganic and organic electrolytes using two-step anodization, Phys. Stat. Sol. 2 (2008) 102-104.

[18] I. Sieber, H. Hildebrand, A. Friedrich, P. Schmuki, Formation of self-organized niobium porous oxide on niobium, Electrochem. Commun. 7 (2005) 97–100.

[19] W. Wei, K. Lee, S. Shaw, P. Schmuki, Anodic formation of high aspect ratio, self-ordered Nb_2O_5 nanotubes, Chem. Commun. 48 (2012) 4244–4246.

[20] K. Yasuda, P. Schmuki, Control of morphology and composition of self-organized zirconium titanate nanotubes formed in $(NH_4)_2SO_4/NH_4F$ electrolytes, Electrochim. Acta 52 (2007) 4053-4061.

[21] A. Ghicov, S. Aldabergenova, H. Tsuchiya, P. Schmuki, TiO_2–Nb_2O_5 nanotubes with electrochemically tunable morphologies, Angew. Chem. Int. Ed. 45 (2006) 6993-6996.

[22] X. Feng, J.M. Macak, P. Schmuki, Flexible self-organization of two size-scales oxide nanotubes on Ti45Nb alloy, Electrochem. Commun. 9 (2007) 2403-2407.

[23] X.J. Feng, J.M. Macak, S.P. Albu, P. Schmuki, Electrochemical formation of self-organized anodic nanotube coating on Ti–28Zr–8Nb biomedical alloy surface, Acta Biomater. 4 (2008) 318-323.

[24] J.M. Macak, H. Tsuchiya, L. Taveira, A. Ghicov, P. Schmuki, Self-organized nanotubular oxide layers on Ti-6Al-7Nb and Ti-6Al-4V formed by anodization in NH_4F solutions, J. Biomed. Mater. Res. A 75 (2005) 928-933.

[25] H. Tsuchiya, J.M. Macak, A. Ghicov, Y.C. Tang, S. Fujimoto, M. Niinomi, T. Noda, P. Schmuki, Nanotube oxide coating on Ti–29Nb–13Ta–4.6Zr alloy prepared by self-organizing anodization, Electrochim. Acta 52 (2006) 94-101.

[26] H. Tsuchiya, J.M. Macak, A. Ghicov, P. Schmuki, Self-organization of anodic nanotubes on two size scales, Small 2 (2006) 888-891.

[27] H. Sopha, A. Jäger, P. Knotek, K. Tesar, M Jarosova, J.M. Macak, Self-organized anodic TiO_2 nanotube layers: influence of the Ti substrate on nanotube growth and dimensions, Electrochim. Acta 190 (2016) 744-752.

[28] J.M. Macak, M. Jarosova, A. Jäger, H. Sopha, M. Klementova, Influence of the Ti microstructure on anodic self-organized TiO_2 nanotube layers produced in ethylene glycol electrolytes, Appl. Surf. Sci., 371 (2016) 607-612.

[29] H. Sopha, L. Hromadko, K. Nechvilova, J.M. Macak, Effect of electrolyte age and potential changes on the morphology of TiO_2 nanotubes, J. Electroanal. Chem. 759 (2015) 122-128.

[30] M. Jin, X. Lu, Y. Qiao, L.-N. Wang, A. A. Volinsky, Fabrication and characterization of anodic oxide nanotubes on TiNb alloys, Rare Met. 35 (2016) 140–148.

[31] K. Zhu, T.B. Vinzant, N.R. Neale, A.J. Frank, Removing structural disorder from oriented TiO_2 nanotube arrays: reducing the dimensionality of transport and recombination in dye-sensitized solar cells, Nano Lett. 7 (2007) 3739-3746.

[32] S.P. Albu, P. Schmuki, TiO_2 nanotubes grown in different organic electrolytes: Two-size self-organization, single vs. double-walled tubes, and giant diameters, Phys. Status Solidi RRL 4 (2010) 215-217.

[33] L. T. Canham, Silicon quantum wire array fabrication by electrochemical and chemical dissolution of wafers, Appl. Phys. Lett. 55 (1990) 1046-1048.

[34] H. Tsuchiya, T. Akaki, D. Terada, N. Tsuji, Y. Minamino, P. Schmuki, S. Fujimoto, Metallurgical aspects on the formation of self-organized anodic oxide nanotube layers, Electrochim. Acta 54 (2009) 5155 - 5162.

[35] Q. Liu, D. Ding, C. Ning, Anodic fabrication of Ti-Nb-Zr-O nanotube arrays, Journal of Nanomaterials, Volume 2014, Article ID 240346.

[36] S.P. Albu, A. Ghicov, S. Aldabergenova, P. Drechsel, D. LeClere, G.E. Thompson, J.M. Macak, P. Schmuki, Formation of double-walled TiO_2 nanotubes and robust Anatase membranes, Adv. Mater. 20 (2008) 4135-4139.

[37] W. Zhang, Z. Xi, G. Li, Q. Wang, H. Tang, Y. Liu, Y. Zhao, L. Jiang, Highly ordered coaxial bimodal nanotube arrays prepared by self-organizing anodization on Ti alloy, Small 5 (2009) 1742–1746.

[38] S. So, I. Hwang, P. Schmuki, Hierarchical DSSC structures based on “single walled” TiO_2 nanotube arrays reach a back-side illumination solar light conversion efficiency of 8%, Energy Environ. Sci. 8 (2015) 849-854.

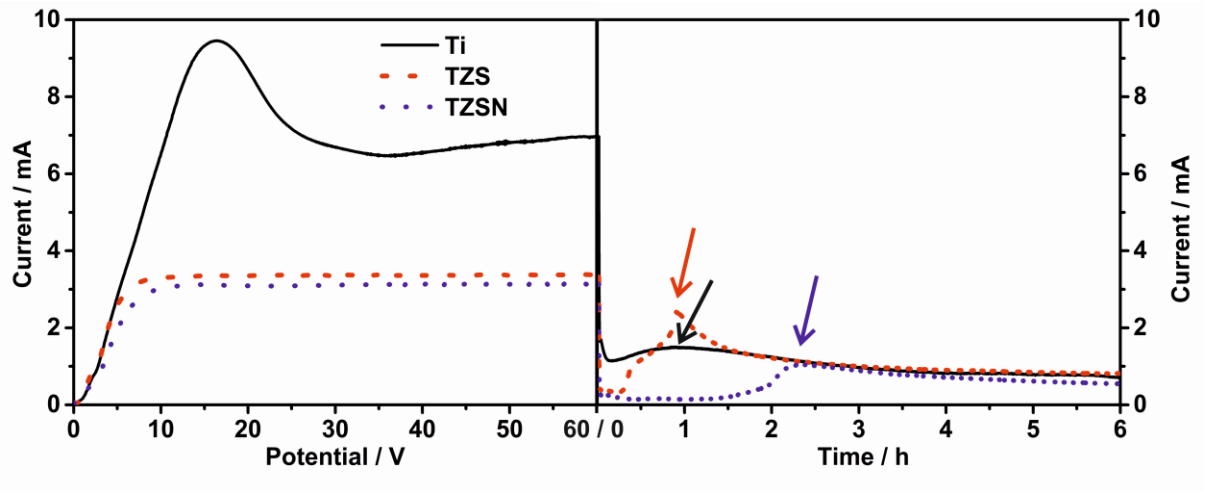

Fig. 1

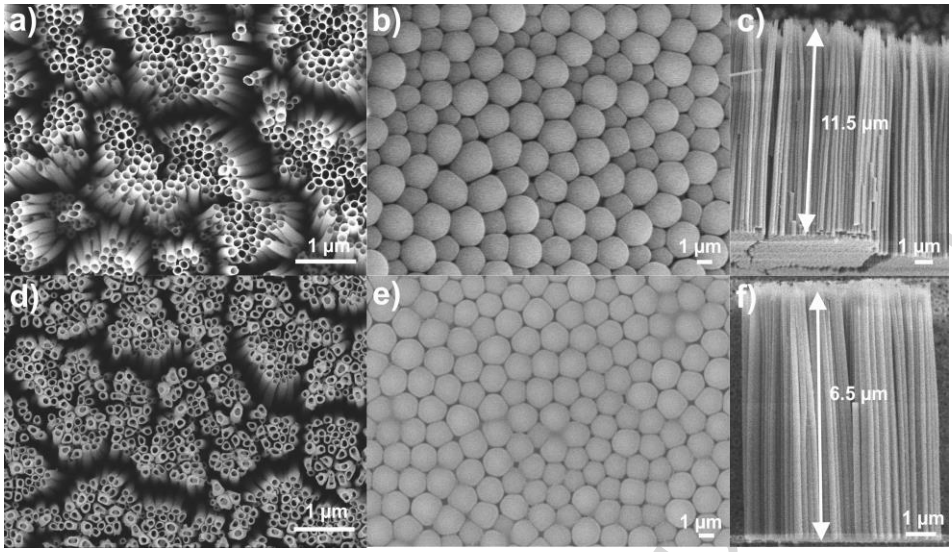

Fig. 2

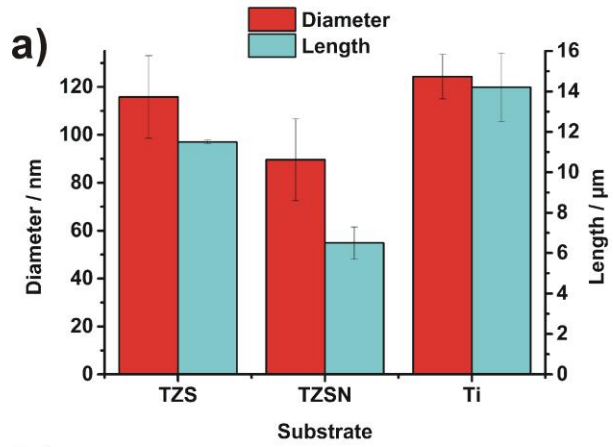

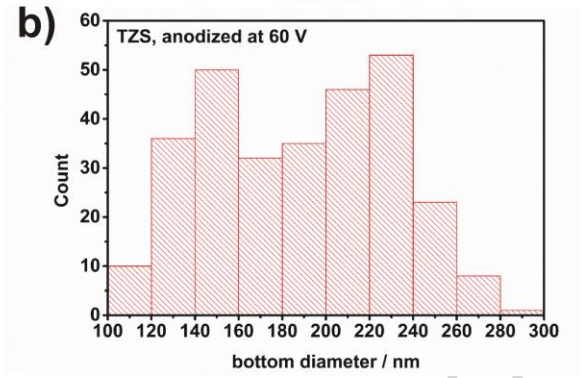

Fig. 3

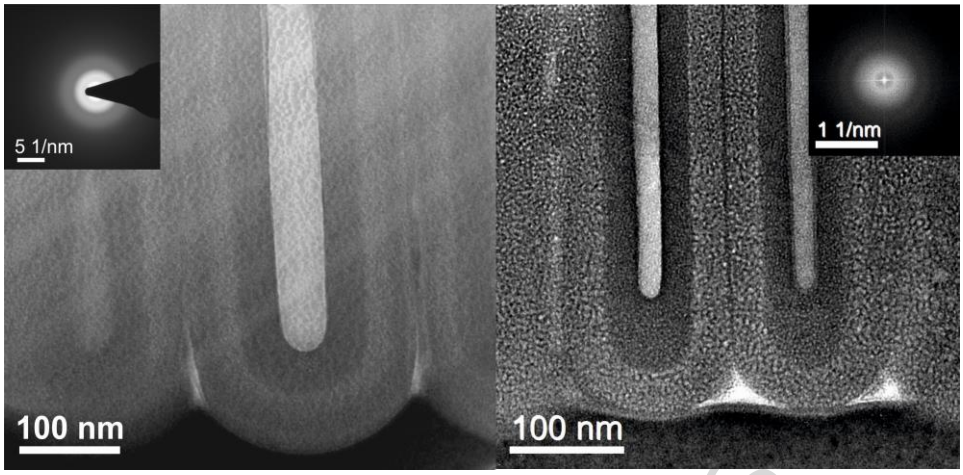

Fig. 4

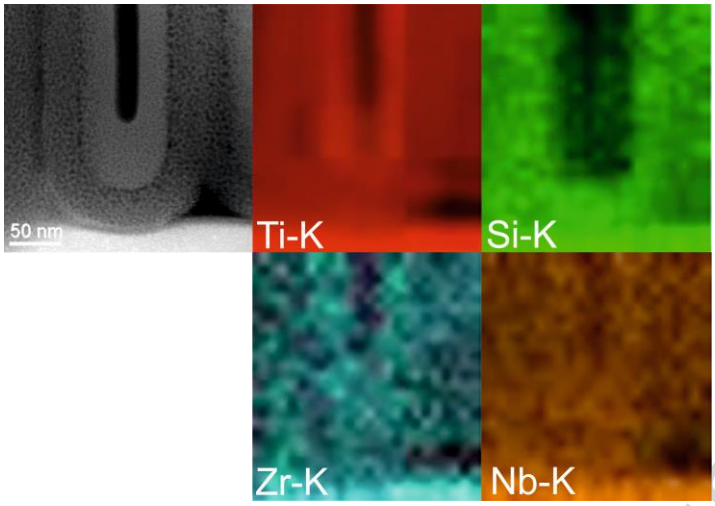

Fig. 5

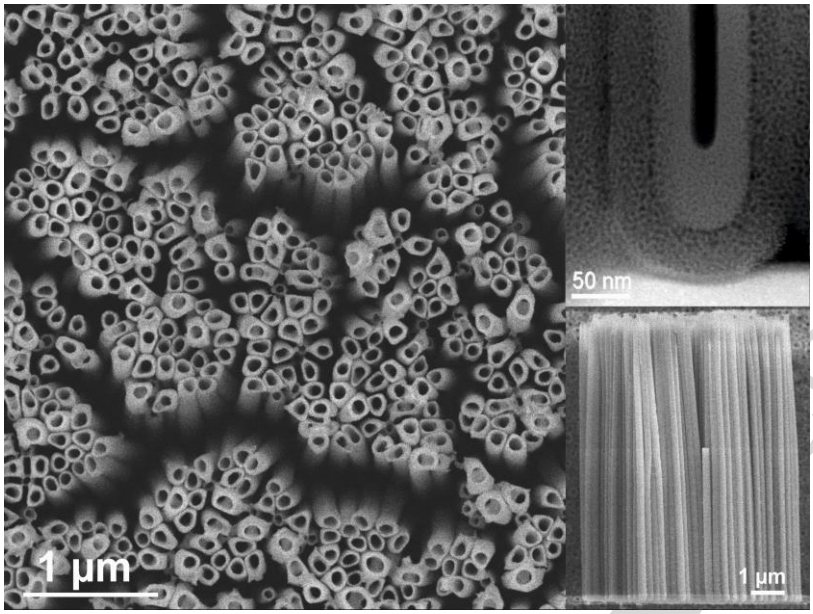

Graphical abstract

Highlights:

- Two amorphous, glass-forming Ti-based alloys were anodized for the first time
- Nanotube layers were obtained on both alloy substrates
- Differences in nanotube dimensions were studied and compared to TiO_2 reference
- Interesting compositional differences within nanotube walls were evaluated by EDX
- HR-TEM analyses revealed a double wall structure